buildings

MDPI

Article

The Effects of Corrugated Steel Fiber on the Properties of Ultra-High Performance Concrete of Different Strength Levels

Vadim Soloviev * and Evgenii Matiushin *

Department of Building Materials, Moscow State University of Civil Engineering, 26 Yaroslavskoye Shosse, 129337 Moscow, Russia

* Correspondence: solovevvg@mgsu.ru (V.S.); matyushinev@mgsu.ru (E.M.)

Abstract: This article describes the influence of corrugated steel fiber on the mechanical properties and fracture energy of Ultra-High Performance Concretes (UHPC) of various strength levels. Three UHPC formulations with compressive strengths of 143, 152, and 177 MPa were tested. The following parameters for the formulations without fiber and those containing 2% steel fiber by volume were determined: compressive strength, splitting tensile strength, flexural strength, modulus of elasticity, Poisson's ratio and critical stress intensity factor. From the axial tensile test results, the following parameters were obtained: the cracking stress, tensile strength, and fracture energy of Ultra-High Performance Fiber Reinforced Concrete (UHPFRC) of different strength levels. With the introduction of steel fiber, an increase in all the investigated parameters is observed regardless of the strength of the concrete matrix. The most remarkable influence the fiber has on the splitting tensile strength, flexural strength and critical stress intensity coefficient, the increase is up to 1.6–3.2 times. There was a slight increase in compressive strength and elastic modulus—up to 5.0–7.4% depending on the composition. Poisson's ratio was equal to 0.2 regardless of the strength of the concrete matrix and the presence of steel fiber. Based on the test results, equations were proposed to predict the properties of UHPC and UHPFRC depending on the water–cement ratio, silica fume content, cement compressive strength and the volumetric content of corrugated steel fiber. The calculated and experimental values showed good convergence with a correlation coefficient in the range of 0.885–0.997.

Keywords: ultra-high-performance concrete (UHPC); ultra-high-performance fiber reinforced concrete (UHPFRC); corrugated steel fiber; mechanical properties; compressive strength; direct tensile strength

check for updates

Citation: Soloviev, V.; Matiushin, E. The Effects of Corrugated Steel Fiber on the Properties of Ultra-High Performance Concrete of Different Strength Levels. *Buildings* **2023**, *13*, 2591. https://doi.org/10.3390/buildings13102591

Academic Editors: Bo-Tao Huang, Jing Yu and Hao-Liang Wu

Received: 19 September 2023
Revised: 11 October 2023
Accepted: 12 October 2023
Published: 13 October 2023

Copyright: © 2023 by the authors. Licensee MDPI, Basel, Switzerland. This article is an open access article distributed under the terms and conditions of the Creative Commons Attribution (CC BY) license (https://creativecommons.org/licenses/by/4.0/).

1. Introduction

Ultra-High Performance Concrete (UHPC) is one of the most up-to-date and efficient types of concrete that simultaneously combines the technologies of High-Strength Concrete (HSC), High Performance Concrete (HPC), and Self-Compacting Concrete (SCC) [1,2]. The minimum compressive strength of UHPC is 150 MPa, and it has significantly higher durability indicators compared to conventional concrete. All these factors are attracting the attention of architects and design engineers around the world. This is evidenced by a number of regulatory documents published in recent decades in countries such as Germany, France, Switzerland, Spain, Australia, Canada, China, Japan, and Korea [3].

The first application of UHPC in the construction of engineering structures took place in 1997 during the construction of a pedestrian bridge in Canada [4]. In 1997–1998, the Cattenom and Civaux nuclear power plants replaced the steel beams in the cooling towers with UHPC precast concrete beams [5]. Despite the aggressive application conditions, the concrete compressive strength increased from 207.8 to 237.7 MPa over 20 years [6]. Today, UHPC is actively used as a material for the manufacture of road and pedestrian bridges [7] and wall panels, as well as for filling joints between precast reinforced concrete structures and repairing and restoring damaged structures [8–10].

To achieve high strength and durability, UHPC is manufactured at extremely low water–cement ratios in the range of 0.15–0.25. To further compact the structure, active and inert mineral additives such as silica fume, blast-furnace granulated slag, fly ash, quartz and limestone powder are introduced into the composition [11]. The maximum aggregate size is limited to 10 mm; however, most UHPC formulations do not contain coarse aggregates. In this case, the grain size does not exceed 1 mm, which also increases the homogeneity of the structure.

To avoid brittle fractures, UHPC is reinforced with steel fiber with a diameter of 0.175–0.3 mm and a length of 6–30 mm. In this case, Ultra-HighPerformance Fiber-Reinforced Concrete (UHPFRC) is obtained. UHPFRC usually contains 1–3% steel fiber by volume. In some cases, its content can reach 11%, for example, in the commercial version of UHPFRC- $CEMTEC_{MULTISCALE}$, which contains fibers of three different sizes [12,13]. The other example is a mix developed at Cardiff University, UK, called CARDIFFRC, which contains 6% steel fiber by volume [14–17]. At present, the production of fibers of various profiles has been industrially established: straight, corrugated, with hooked ends, as well as twisted with triangular cross-section. Fibers with a deformed profile have a higher bond strength to concrete. This leads to higher values of both compressive and tensile strength.

The introduction of steel fiber into the composition leads to an increase in the mechanical characteristics of the material, as well as the appearance of residual strength. Depending on the type and volumetric content of steel fibers, the compressive strength of UHPC can increase by up to 1.5 times [18–26]. In ref. [19], the influence of straight steel fiber with different length-to-diameter ratios on the compressive strength of UHPFRC was investigated. The results show that when using fibers with l_f/d_f=100, an increase in its volumetric content from 0 to 3% leads to an increase in strength from 135 to 182 MPa, while fiber with l_f/d_f = 30 at the same volume content increases the strength up to 156.5 MPa. Similar results were obtained by the authors of research [23], which investigated the change in the strength of UHPFRC with hooked end fibers. One of the advantages of UHPFRC isits high tensile strength, the values of which are in the range of 8–21 MPa at fiber contents up to 3% [27–30] and up to 35 MPa at a fiber content of 6% [31]. The material also has high fracture energy, which, depending on the volumetric content and orientation of the fiber, is in the range of 20–94.1 kJ/m^3 [32–35]. The flexural strength of UHPFRC is in the range of 10–50 MPa with a fiber volume content of up to 3% [36–38]. The modulus of elasticity also increases with the introduction of steel fiber. The increase is about 5–17%, depending on the fiber volume fraction [39–41].

In the vast majority of cases, UHPFRC is reinforced with straight steel fibers with fiber lengths of up to 20 mm. The effective performance of straight fibers in UHPFRC is possible due to the very dense contact zone between the fiber surface and the concrete. The bond strength of straight steel fiber with UHPC is in the range of 5–20 MPa with a matrix strength of 100–250 MPa [42–46]. In comparative tests of different types of fibers with a concrete matrix of the same strength level, hooked end fibers show 2–4 times higher bond strength compared to straight fibers [47,48]. The disadvantages of such fibers include the tendency to clump, which is not observed in straight fibers, even at high volume content.

In the territory of the Russian Federation, corrugated steel fiber is the most widespread. To date, relatively few works have been devoted to the study of UHPFRC with this type of fiber. The purpose of this research was to study the influence of corrugated steel fiber on the mechanical properties and fracture energy of UHPFRC of various strength levels.

2. Materials and Methods

2.1. Raw Materials

Gray Portland cement CEM II/A-L 42.5 and CEM I 52.5 and white Portland cement were used as binders. The main physical characteristics and mineralogical composition of the cements are given in Table 1.

Table 1. Properties of cementitious materials.

Cement ID	Density, kg/m^3	Fineness, m^2/kg	28 Days Compressive Strength, MPa	C_3S, %	C_2S, %	C_3A, %	C_4AF, %
C_1	2960	468.2	48.3	69.9	8.4	4.9	12.5
C_2	3110	409.3	56.0	60.4	8.07	4.9	11.7
C_3	3100	497.1	66.5	70.8	19.5	6.0	1.0

Quartz sand of fractions 0.1–0.4 and 0.4–0.8 was used as the aggregate. The ratio between the fractions was selected based on the maximum packing density of the particles. The higher packing density of particles enables increasing the workability of the concrete mixture due to the formation of a thicker layer of cement paste around the grains [11]. The particle size distribution of the aggregate was optimized using the Compressible Packing Model (CPM) developed by F. De Larrard [49]. Among the other similar models, CPM is characterized by high convergence with experimental data [50]. This is achieved by using the real packing density of each fraction and by using the compaction index, reflecting the mechanical impact on the particles during their placement in the container. The findings from article [51], in conjunction with CPM, can be used to calculate the packing density of the aggregate, taking into account the influence of the steel fibers. Table 2 summarizes the main characteristics of the aggregate required for the calculation. The graph in Figure 1 shows the relationship between the packing density of the mixture and the content of the fraction 0.1–0.4. The highest packing density is achieved at the content of 0.1–0.4 fraction of 30%.

Table 2. Properties of aggregates.

Fraction	Density, kg/m^3	Bulk Density, kg/m^3	Mean Particle Size, mm	Packing Density, -
0.1–0.4	2637	1403	0.25	0.532
0.4–0.8	2632	1524	0.60	0.579

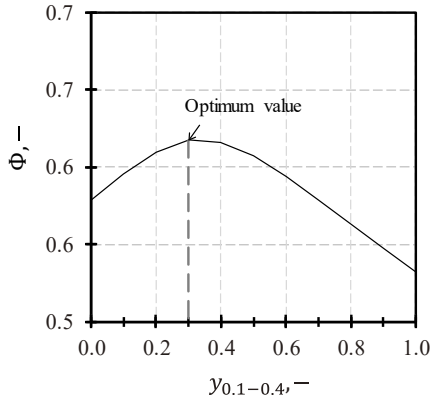


Figure 1. Packing density of binary mixture.

Table 3 summarizes the properties of the mineral additives used in this research. The content of silica in quartz powder and calcium carbonate in limestone powder is more than 95%. The content of amorphous silica in silica fume is ≥85%.

Table 3. Properties of powder materials.

Powder	Density, kg/m^3	Fineness, m^2/kg
Limestone powder (LP)	2715	281.2
Quartz powder (QP)	2650	429.6
Silica fume (SF)	2200	17000

The brass-coated corrugated steel fiber made of high-carbon steel wire was used. The length and diameter of the fiber are 15 and 0.3 mm, respectively ($l_f/d_f = 50$). The tensile strength is not less than 1800 MPa. The appearance of steel fiber is shown in Figure 2.



Figure 2. Steel fiber used in this study.

A superplasticizer based on polycarboxylate esters, Sika ViscoCrete 24HE, with a density of 1075–1095 kg/m^3, was used to produce a self-compacting concrete mix.

2.2. Mix Design

In this work, 3 concrete compositions with target compressive strengths of 130, 150 and 170 MPa of plain matrix were developed, which are hereafter designated as I, II and III, respectively. To study the effect of steel fiber on the properties of UHPFRC, 2% steel fiber by volume was added to each formulation. The resulting compositions are designated I-F, II-F and III-F. The consumption of components per 1 m^3 is presented in Table 4.

Table 4. Mixture proportions of studied mixtures.

Component	I	II	III	I-F	II-F	III-F
C_1	850	-	-	832	-	-
C_2	-	796	-	-	780	-
C_3	-	-	803	-	-	787
LP	213	-	-	208	-	-
QP	-	200	200	-	195	197
SF	128	200	200	125	195	197
Sand 0.1–0.4	295	285	290	287	280	283
Sand 0.4–0.8	685	670	675	670	655	661
Water	195	191	177	191	187	173
SP	26	29	36	29	31	39
Steel fiber	-	-	-	156	156	156
W/C	0.23	0.24	0.22	0.23	0.24	0.22
SP/C	0.031	0.036	0.045	0.035	0.040	0.050
SF/C	0.15	0.15	0.25	0.15	0.25	0.25

The water–cement ratio in all compositions was in the range of 0.22–0.24. The mix I was made using C_1 cement and limestone powder as inert filler; the silica fume content was 15% of the cement weight. Mixtures II and III were made using C_2 and C_3 cement, respectively. In both mixtures, silica powder was used as an inert filler. The silica fume content was 25% of the cement weight.

The content of superplasticizer and aggregate in all mixes was selected in such a way as to ensure the slump flow of the mixture was in the range of 230–250 mm on the Hagermann cone.

2.3. Mix Preparation

The Viatto B-30P mixer with planetary paddle rotation was used for the preparation of concrete mixtures. Mixing of components was carried out in the following sequence: (1) mixing of dry components for 2 min at a speed of 105 rpm; (2) addition of water and 70% of plasticizing admixture and mixing for 5 min at a speed of 105 rpm; (3) addition of the remaining plasticizing admixture and mixing to a homogeneous state at a speed of 408 rpm for 5–8 min.

After molding, the samples were stored in laboratory conditions at 20 °C for 24 h. To avoid moisture evaporation, the exposed surface of the specimens was covered with a polyethylene film. After 24 h, the samples were unmolded and stored for the next 24 h under normal conditions. After 48 h from the date of fabrication, the samples were placed in a heat and humidity treatment chamber and kept at 80 °C for 48 h. After heat treatment, the specimens were stored in the laboratory room for 72 h until testing.

2.4. Experimental Methods

2.4.1. Compressive Strength

The compressive strength of the specimens was determined on cube specimens of 70 × 70 × 70 mm according to the Russian standard GOST 10180-2012 [52]. The specimens were loaded at a rate of 2 MPa/s. The compressive strength of each specimen was determined by Equation (1):

$$f_{c,i} = F/A, \text{ [Mpa]} \quad (1)$$

where

F—maximum force, N;
A—cross-sectional area, mm^2.

The compressive strength of each composition was determined as the arithmetic mean of the results of 6 parallel tests.

2.4.2. Splitting Tensile Strength

The splitting tensile strength was determined on cube specimens of 70 × 70 × 70 mm according to the Russian standard GOST 10180-2012. The specimens were loaded at a rate of 0.05 MPa/s. The test scheme is shown in Figure 3. The ultimate strength of each specimen was determined through the use of Equation (2):

$$f_{ct,sp,i} = 2 \cdot F/\pi \cdot A, \text{ [Mpa]} \quad (2)$$

where

F—maximum force, N;
A—cross-sectional area, mm^2.

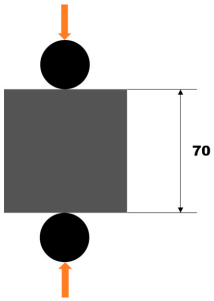


Figure 3. Splitting tensile strength determination scheme.

The splitting tensile strength of each composition was determined as the arithmetic mean of the results of 6 parallel tests.

2.4.3. Flexural Strength

The flexural strength was determined by testing prismatic specimens of 70 × 70 × 280 mm for 4-point bending according to the Russian standard GOST 10180-2012 [52]. The loading rate of the specimens was 0.05 MPa/s. The distance between the bottom supports was 210 mm. The flexural strength of each specimen was determined through the use of Equation (3):

$$f_{ct,fl,i} = F \cdot L / b \cdot h^2, \text{ [Mpa]} \quad (3)$$

where

F—maximum force, N;
L is the distance between supports, mm;
b, h is the width and height of cross-section, mm.

The flexural strength of each composition was determined as the arithmetic mean of the results of 6 parallel tests.

2.4.4. Modulus of Elasticity and Poisson's Coefficient

The modulus of elasticity and Poisson's ratio were determined according to the Russian standard GOST 24452-80 [53]. Prism specimens with dimensions of 70 × 70 × 280 mm were used for the tests. Longitudinal and transverse strains were measured using digital sensors mounted on 4 faces of the specimen (Figure 4).



Figure 4. Test setup for determination of modulus of elasticity and Poisson's coefficient.

The modulus of elasticity and Poisson's ratio were determined using Equations (4) and (5) at a stress equal to 0.3 of the prismatic strength of the concrete:

$$E_c = \sigma_c / \varepsilon_{1,m}, \text{ [Mpa]} \quad (4)$$

$$\nu_c = \varepsilon_{2,m} / \varepsilon_{1,m}, \text{ [}-\text{]} \quad (5)$$

where

σ_c is the compressive stress equal to 30% of the prismatic compressive strength, MPa;
$\varepsilon_{1,m}$ и $\varepsilon_{2,m}$ is the average longitudinal and transverse deformation at a stress level of 30% of the prismatic compressive strength.

The result of the test was the arithmetic mean of 6 parallel measurements.

2.4.5. Critical Stress Intensity Factor

The critical stress intensity factor, $K_{I,c}$, was determined on 40 × 40 × 160 mm prismatic specimens with an artificial crack, which was formed by embedding a 40 × 10 × 0.5 mm

steel plate during specimen fabrication. The test scheme is shown in Figure 5. The loading rate of the specimens was 0.1 mm/s. The critical stress intensity factor for each specimen was calculated by Equation (6) according to the Russian standard GOST 29167-2021 [54]:

$$K_{I,c} = \frac{1.5 \cdot F \cdot L}{b^{3/2} \cdot t} \cdot \sqrt{a_0 \cdot b} \cdot \left(1.93 - 3.07 \cdot \lambda + 14.53 \cdot \lambda^2 - 25.11 \cdot \lambda^3 + 25.8 \cdot \lambda^4, \left[\text{MPa} \cdot \sqrt{\text{m}}\right]\right) \quad (6)$$

where

F is the force at cracking, MN;
L is the distance between supports, m;
b, t is the height and width of cross-section, m;
a_0 is the notch depth, m;
$\lambda = a_0 / b$.

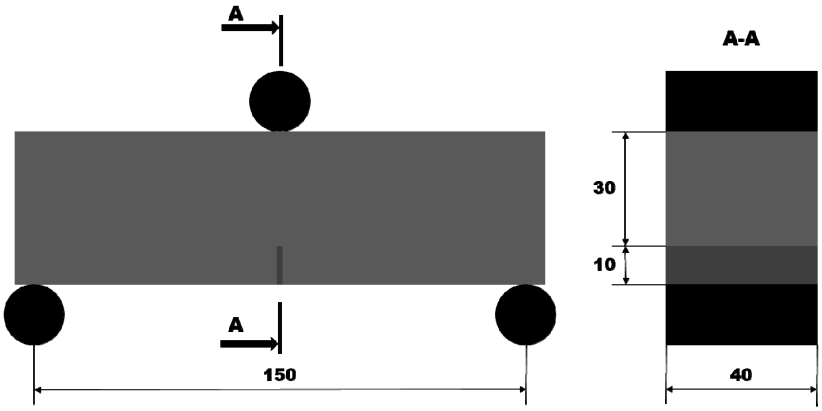


Figure 5. Critical stress intensity factor determination scheme. Dimensions are expressed in millimeters.

2.4.6. Axial Tensile Strength

The mixtures containing steel fiber were tested for axial tensile strength. The test was carried out on dog-bone-shaped samples with a cross-section of 50 × 30 mm in the working part. The geometric dimensions of the specimens are presented in Figure 6a. After heat treatment, the upper part of the specimens was ground. In order to avoid stress concentration in the gripping zone of the specimen, 100 × 55 mm plywood plates were applied to the end parts of the specimen from the front and back sides.

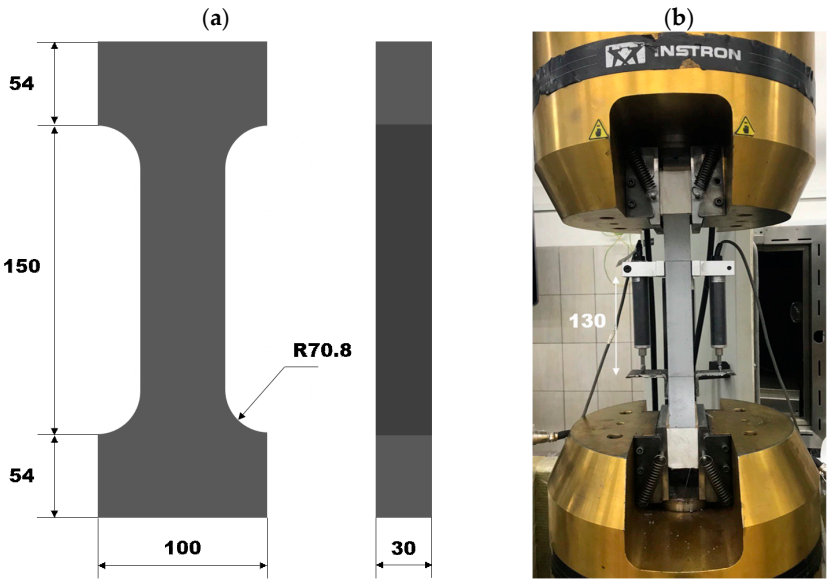


Figure 6. (**a**) Shape and dimensions (in millimeters) of test specimens; (**b**) Specimen in the testing machine.

The tensile strains of the specimen were determined using 2 digital displacement sensors located on two opposite faces. The measurement base was 130 mm. The appearance of the specimen in the testing machine is shown in Figure 6b.

The loading rate was 0.2 mm/min. The cracking strength, $f_{ct,cr}$, was determined at the moment of the appearance of the first crack in the specimen, which characterizes the end of the elastic part of the material. After the appearance of the first microcrack in UHPFRC with fiber volume content of more than 1.5–2%, as a rule, the region of strain-hardening characterized by the formation of many microcracks along the entire length of the specimen begins. Tensile stress continues to increase at the same time. The end of this region is the strength at the moment of strain localization, $f_{ct,loc}$, which characterizes the beginning of the opening of one of the previously formed microcracks with the gradual pulling of the fiber out of the concrete. At the same time, a gradual decrease in tensile stress is noted on the deformation diagram.

Three specimens were tested for each composition. According to the test results, an averaged stress–strain diagram was constructed, from which the parameters $f_{ct,cr}$ and $f_{ct,loc}$ were determined. The values of fracture energy were also determined, which for this class of materials consists of two components [34,35]: (1) $g_{f,\,A}$ is the amount of energy dissipated per unit volume of UHPFRC in the process of strain-hardening, determined by integrating the curve "σ-ε" up to the value of relative strain corresponding to the value of $f_{ct,loc}$; (2) $G_{f,\,B}$ is the amount of energy dissipated to completely separate the UHPFRC into two parts, determined by integrating the curve "σ-w" up to the value of crack opening $w = l_f/4$. To construct the complete "σ-w" diagram, the experimental data were approximated to the value of w = 15/4 = 3.75 using the following equation [55]:

$$\sigma_t = f_{ct,loc} \cdot \left(1 - \frac{4 \cdot w}{l_f}\right)^n, \text{ [MPa]} \quad (7)$$

where
$f_{ct,loc}$ is the tensile strength of UHPFRC, MPa;
w is the crack opening, mm;
l_f is the fiber length, mm;
N is the degree index taking values in the range of 2–3.

Figure 7 shows the scheme of determination of strength and fracture energy.

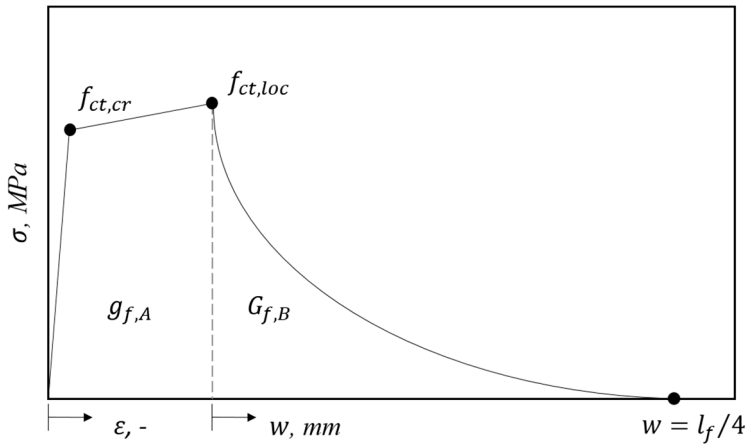


Figure 7. Schematic representation for determination of strength and fracture energy of UHPFRC.

3. Results and Discussion

The results of the tests performed are summarized in Table 5. The discussion of the results is presented in the following sections.

Table 5. Test results.

Property	I	I-F	II	II-F	III	III-F
f_c, MPa	143.4	152.1	152.3	163.6	177.0	189.8
$f_{ct,sp}$, MPa	6.52	11.44	6.72	12.45	8.79	14.20
$f_{ct,fl}$, MPa	9.13	24.04	10.68	25.51	15.26	28.43
$f_{ct,cr}$, MPa	-	7.43	-	8.51	-	9.03
$f_{ct,loc}$, MPa	-	8.49	-	9.87	-	11.55
$g_{f,A}$, kJ/m^3	-	8.06	-	23.81	-	28.12
$G_{f,B}$, kJ/m^2	-	9.02	-	11.63	-	14.10
E_c, GPa	44.4	47.4	43.3	46.2	47.1	49.6
ν_c, -	0.22	0.21	0.19	0.19	0.20	0.19
$K_{I,c}$, MPa·$\sqrt{\text{m}}$	0.929	2.856	1.001	3.122	1.164	3.353

3.1. Compressive Strength

Figure 8 shows the results of compressive strength of the tested compositions.

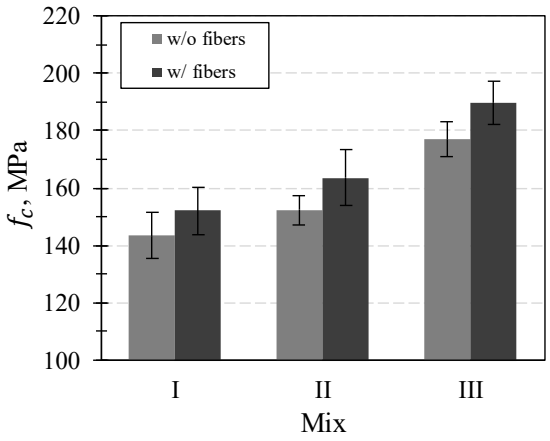


Figure 8. Effect of steel fiber addition on compressive strength of different UHPC mixes.

The compressive strength of concrete without steel fiber was 143.4, 152.3 and 177.0 MPa for compositions I, II and III, respectively. The difference in strength is due to the use of types of cement with different specific surface areas and different amounts of silica fume. The silica fume reacts with portlandite formed during cement hydration to form calcium silicate hydrates (CSHs), which increase the density and strength of the contact zone between aggregate and cement paste, resulting in higher compressive strength [56]. An increase in the specific surface area of cement, all other things being equal, results in a higher degree of hydration of the clinker, which results in more water being chemically bound and produces a structure with a lower pore content. The content of silica fume in composition I was 15% of the cement weight, and the cement compressive strength was 48.7 MPa, which resulted in the lowest strength. Compositions II and III contained 25% silica fume and cements with compressive strength of 56.0 and 65.5 MPa, resulting in strength increases of 6.2 and 17.2% compared to composition I.

The addition of steel fiber in the amount of 2% by volume resulted in a slight increase in compressive strength for all the mixtures tested in this work, which is in agreement with the results obtained by other authors [18,22]. The compressive strength of UHPFRC with steel fiber was 152.1, 163.6 and 189.8 MPa for compositions I-F, II-F and III-F, respectively, which is higher by 6.1, 7.4 and 7.2% compared to the plain UHPC without steel fiber. This is explained by the fact that the fiber prevents the development of microcracks during loading, which leads to an increase in the maximum stress that the material is able to withstand.

3.2. Indirect Tensile Strength

Figure 9 shows the results of splitting tensile strength and flexural strength.

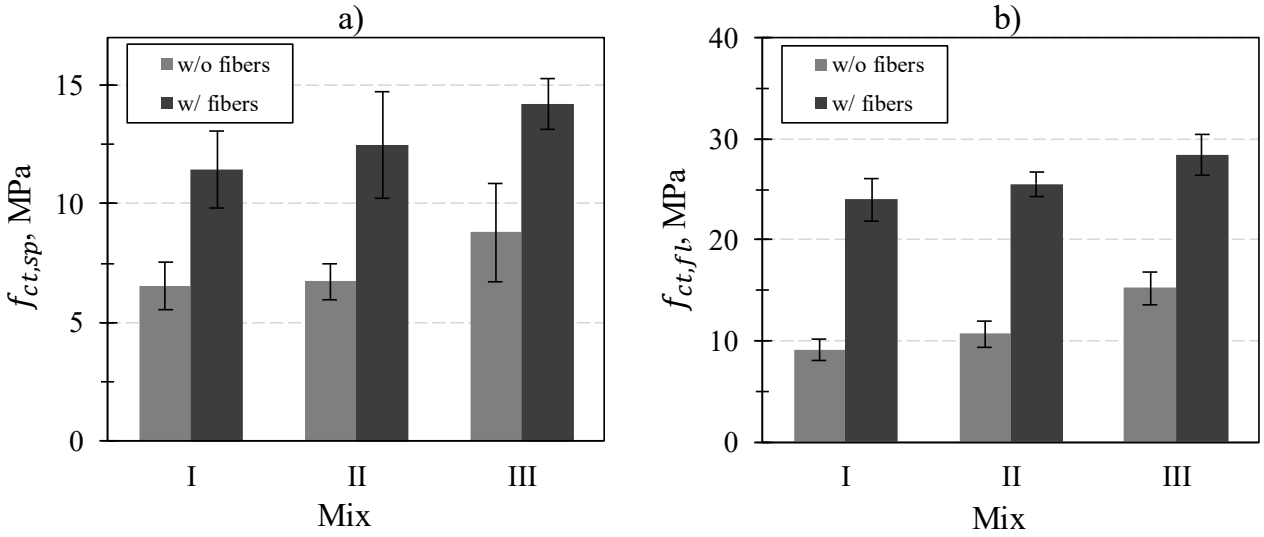


Figure 9. Effect of steel fiber addition on indirect tensile strength of different UHPC mixes: (**a**) splitting tensile strength; (**b**) flexural strength.

The data in Figure 8 show a similar trend compared to the compressive strength. Thus, the splitting tensile strength for plain UHPC without steel fiber was 6.52, 6.72 and 8.79 MPa, and the flexural strength was 9.13, 10.68 and 15.26 MPa for compositions I, II and III, respectively.

The splitting tensile strength of UHPFRC was 11.44, 12.45 and 14.20 MPa for compositions I-F, II-F and III-F, respectively, which is higher than 75, 85 and 62% as compared to plain UHPC. The flexural strength was 24.04, 25.51 and 28.43 MPa for compositions I-F, II-F and III-F, respectively, which is higher by 163, 139 and 86% as compared to plain UHPC.

The obtained data are consistent with the results obtained by other authors. In ref. [57], it was found that the introduction of 2% straight steel fiber leads to an increase in flexural strength by 23–57% and splitting tensile strength by 122–159% depending on the l_f/d_f ratio of the fiber. In the article [37], UHPFRC specimens with straight and hooked-end fibers with l_f/d_f ratios of 65–100 and 80–100, respectively, were tested. The flexural strength at 2% fiber content increased by 180–290% for straight fiber and 165–229% for hooked-end fiber.

A significant increase in strength with the introduction of steel fiber can be explained as follows: steel fiber has about 4–5 times higher modulus of elasticity compared to the concrete matrix. Via tension, steel fibers absorb a part of the arising stresses, unloading the concrete matrix and increasing the composite strength. On the other hand, in order to fracture the UHPFRC, it is necessary to use additional force to pull the fibers out of the concrete matrix, which also gives an additional increase in strength.

3.3. Modulus of Elasticity and Poisson's Coefficient

Figure 10 shows the results of determining the elastic modulus and Poisson's ratio.

The modulus of elasticity of plain UHPC was 44.4, 43.3 and 47.1 GPa for compositions I, II and III, respectively.

The modulus of elasticity of UHPFRC is 47.4, 46.2 and 49.6 GPa, which is 6.8, 6.7 and 5.3% higher compared to the unreinforced matrix. The increase in values is due to the fact that steel has a higher modulus of elasticity compared to concrete. The obtained results correspond to the calculated values, which can be obtained according to the known «rule of mixtures» [58].

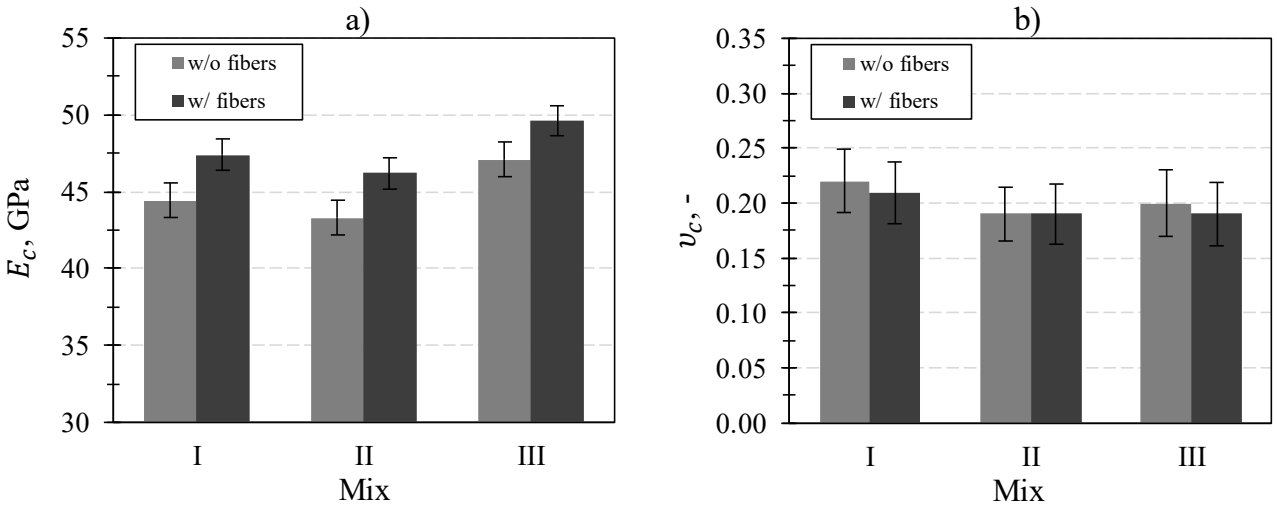


Figure 10. Effect of steel fiber addition deformability of different UHPC mixes: (**a**) modulus of elasticity; (**b**) Poisson's coefficient.

The graph in Figure 11 shows the relationship between the compressive strength and modulus of elasticity of UHPC. The results of the calculation of the UHPC modulus of elasticity using the formulas from the works [59–61] are also presented (Table 6).

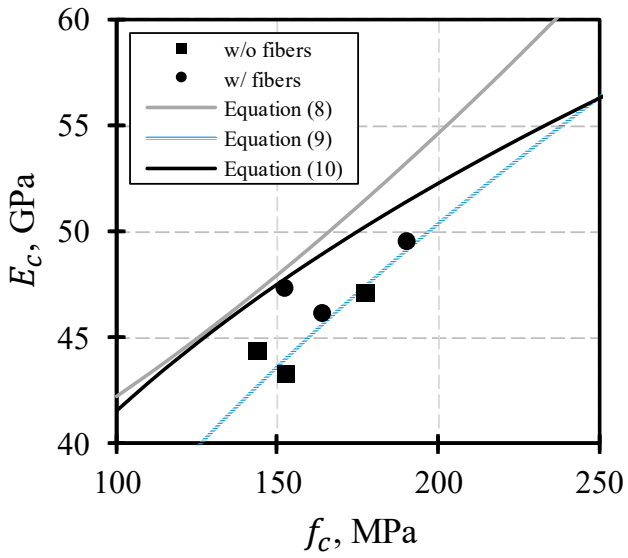


Figure 11. Relationship between modulus elasticity and compressive strength of UHPC with and without steel fiber.

Table 6. Equations proposed for calculating the modulus of elasticity of UHPC.

Compressive Strength Range, MPa	Equation		References
38–235	$E_c = \left(9 \cdot (f_c)^{1.45} + 35,120\right)/1000$	(8)	[59]
120–256	$E_c = 3.565 \cdot (f_c)^{0.5}$	(9)	[60]
127–200	$E_c = \left(9100 \cdot (f_c)^{0.33}\right)/1000$	(10)	[61]

The best convergence with the actual values is shown by Equation (9), which can be recommended for use for approximate determination of the UHPC modulus of elasticity.

The value of Poisson's ratio practically does not depend on the compressive strength of concrete and the presence of steel fiber in the composition. The average value of Poisson's

ratio for all compositions in this study is 0.2. In ref. [61], the results of tests of 102 UHPC compositions with compressive strength in the range of 80–200 MPa are presented, where no correlation between strength and Poisson's ratio was found. The arithmetic mean value was 0.14 ± 0.029. The authors of the paper proposed to use the value of 0.15, which is 33% lower than the results obtained in this work.

3.4. Critical Stress Intensity Factor

Figure 12 shows the results of determining the critical stress intensity factor.

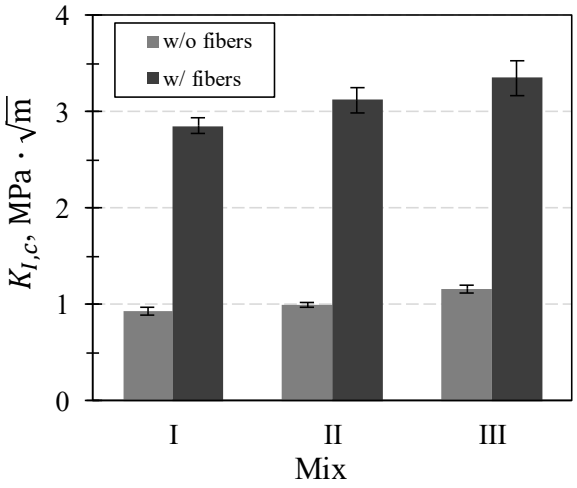


Figure 12. Effect of steel fiber addition on critical stress intensity factor of different UHPC mixes.

The critical stress intensity factor of the plain UHPC was 0.929, 1.000 and 1.164 MPa·$\sqrt{m}$ for compositions I, II and III, respectively. The slight increase in the value of $K_{I,c}$ is due to the decrease in water–cement ratio as well as the increase in cement compressive strength, which together lead to a decrease in porosity. Despite its high compressive strength, UHPC has the same or slightly lower $K_{I,c}$ value compared to ordinary heavy concrete. In refs. [62,63], $K_{I,c}$ was determined for coarse aggregate concrete with compressive strength in the range of 50–70 MPa, for which the value of $K_{I,c}$ varied in the range of 0.986–1.402. The higher stress intensity factor in conventional coarse aggregate concrete compared to UHPC is explained by more than 2 times higher volume content of aggregate. The aggregate particles increase the critical stress intensity factor by inhibiting or deflecting the microcracks formed during loading [64]. In addition, the porous contact zone further reduces the stress intensity near the crack tip.

When steel fiber is incorporated, a sharp increase in $K_{I,c}$ is observed, which was 2.856, 3.122 and 3.353 MPa·$\sqrt{m}$ for compositions I-F, II-F and III-F, respectively, which is 3.07, 3.12 and 2.88 times higher compared to plain UHPC. This significant increase in $K_{I,c}$ is because the fibers cross the crack formed; for further growth, a force must be applied to pull the fibers out of the concrete [65].

3.5. Direct Tensile Test

Figure 13 shows the stress–strain and stress–crack opening diagrams for the tested UHPFRC formulations. The experimentally obtained diagram averaged from the test results of three specimens is shown in gray, and the approximate results are shown in black. The solid line shows the bilinear diagram up to the stress value $f_{ct,loc}$, the dashed line shows the "σ_t-w " relationship calculated by Equation (7).

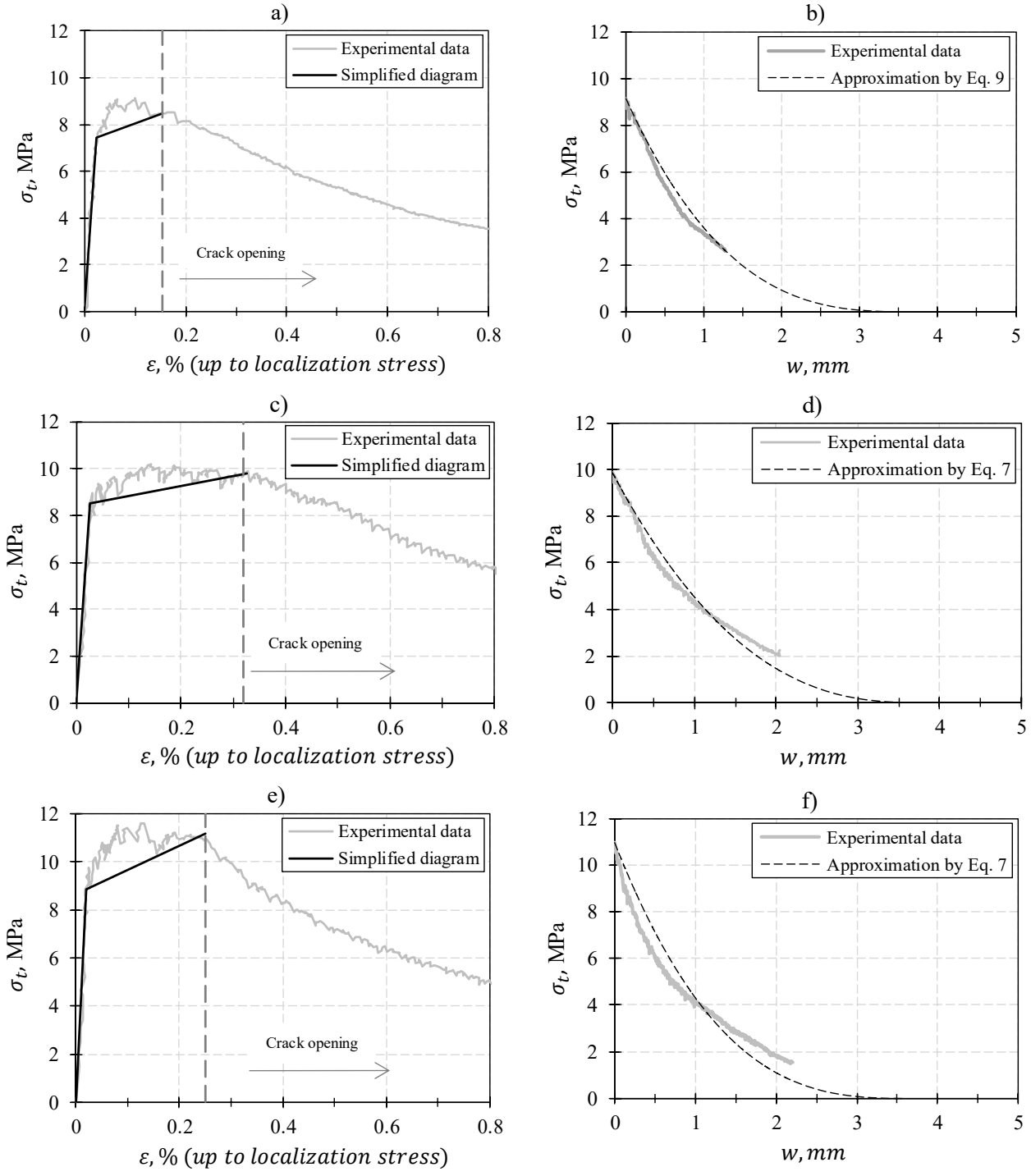


Figure 13. Direct tensile test results: (**a**,**b**) stress–strain and stress–crack opening for mix I-F; (**c**,**d**) stress–strain and stress–crack opening for mix II-F; (**e**,**f**) stress–strain and stress–crack opening for mix III-F.

The tested compositions belong to the strain-hardening class (the ratio $\gamma = f_{ct,loc}/f_{ct,cr}$ was 1.14, 1.16 and 1.28 for compositions I, II and III, respectively). After the elastic part of the material work and the formation of the first crack, the stress in the specimen continued to increase, which was accompanied by the formation of microcracks along the entire length of the specimen. This is explained by the fact that in the section with the crack there is a large number of fibers and the force that must be applied to pull them out is higher than the force to fracture the concrete matrix, which leads not to further crack opening, but to

the formation of a new crack. The number of potential microcracks depends on the length of the fibers and the length of the tensile element and is determined by the equation [66]:

$$N = \frac{4 \cdot l_{elm}}{3 \cdot l_f}, \ [-] \tag{11}$$

where l_{elm} is the tensile member length.

Microcracking stops at the moment when all possible cracks have been formed. Under further loading, stresses are localized in one of the previously formed cracks, which leads to gradual pulling out of the fiber and reduction in tensile stress.

Figure 14 shows the values of $f_{ct,cr}$ and $f_{ct,loc}$ for the tested compositions.

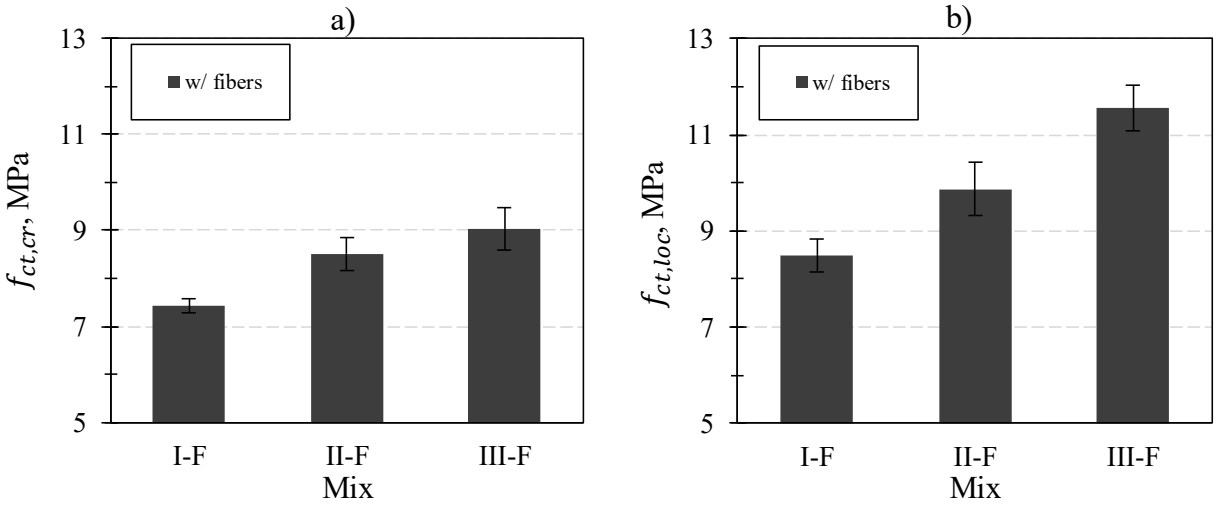


Figure 14. Results of the direct tensile test: (**a**) $f_{ct,cr}$; (**b**) $f_{ct,loc}$.

The stress at the moment of the first crack formation, $f_{ct,cr}$, was 7.43, 8.51 and 9.03 MPa for compositions I-F, II-F and III-F, respectively. The value of $f_{ct,cr}$ of UHPFRC with a given volume content of steel fibers is determined through the tensile strength of the plain UHPC because the fiber remains inactive until a crack is formed. The contribution of steel fiber to cracking stress is about 3% according to [66]. A regular increase in $f_{ct,cr}$ with increasing concrete matrix strength was found for different compositions.

The axial tensile strength of UHPFRC, $f_{ct,loc}$, was 8.49, 9.87 and 11.55 MPa for compositions I, II and III, respectively. The post-cracking tensile strength of fiber reinforced concrete depends on a number of factors and is determined by the following equation [55]:

$$f_{ct,loc} = \alpha_0 \cdot \alpha_1 \cdot \tau_f \cdot V_f \cdot \frac{l_f}{d_f}, \ [\text{Mpa}] \tag{12}$$

where

α_0 is the fiber orientation factor;
α_1 is the fiber efficiency factor;
τ_f is the fiber-to-matrix bond strength, MPa;
V_f is the fiber volume fraction;
l_f, d_f is the length and diameter of fiber, mm.

The fiber orientation factor, α_0, is defined as the probability of a single fiber being intersected by a random section plane. The fiber efficiency factor, α_1, is a parameter that accounts for the dependency of the fiber pull-out force with the orientation angle θ (i.e., the angle of the fiber with the normal to the fracture surface). Considering that all the mixtures contained fibers with the same $\frac{l_f}{d_f}$ and V_f and the same casting method, the difference

in strength can be explained by the higher τ_f in the compositions with stronger concrete matrix.

Figure 15 shows the results of fracture energy $g_{f,\,A}$ and $G_{f,\,B}$.

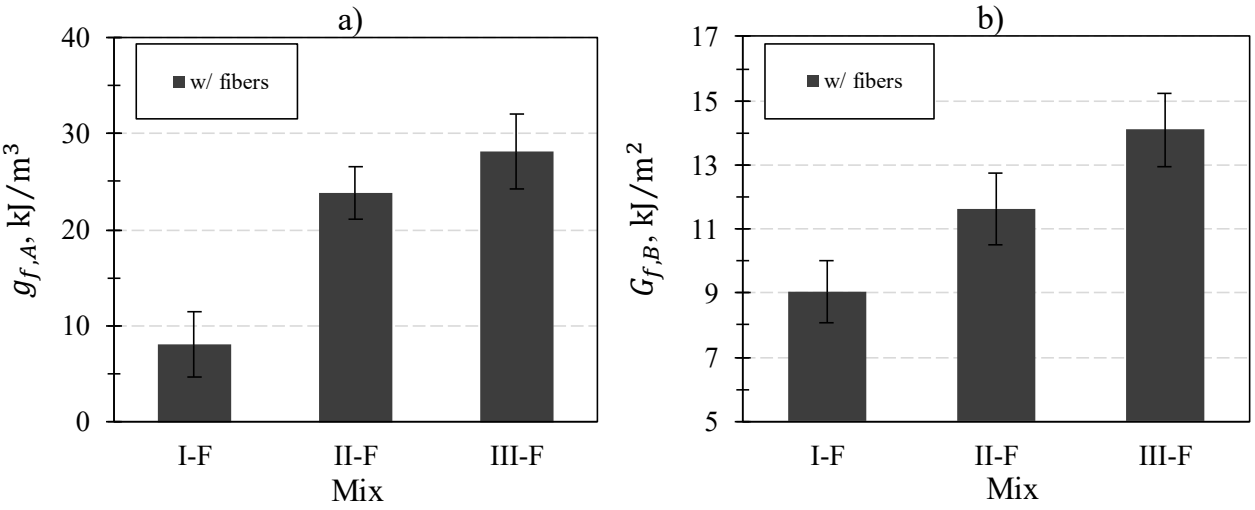


Figure 15. Fracture energy of UHPFRC's: (**a**) $g_{f,\,A}$; (**b**) $G_{f,\,B}$.

The amount of energy dissipated per unit volume of material, $g_{f,\,A}$, was 8.06, 23.81 and 28.12 kJ/m^3 for formulations I, II and III, respectively. The fracture energies of compositions II and III are 3 and 3.5 times higher compared to composition I. This is probably due to the higher content of silica fume, which provided the formation of a stronger contact zone between the concrete matrix and fiber. In the works [67,68], it was found that the introduction of silica fume in the amount of 15–20% in the composition leads to an increase in the bond strength by 2.3–4.5 times. In compositions II and III, cement with higher specific surface area was also used, which at approximately equal values of W/C provides a greater degree of clinker hydration and formation of an additional amount of CSH, increasing the bond with fiber. The higher bond strength ensures the formation of more microcracks along the length of the specimen during axial tension, for which additional energy must be dissipated.

The amount of energy dissipated per unit cross-sectional area, $G_{f,\,B}$, was 9.02, 11.63, and 14.10 kJ/m^2 for formulations I-F, II-F, and III-F, respectively. The increase in $G_{f,\,B}$ was associated with higher peak stress value, $f_{ct,loc}$.

4. Practical Recommendations

According to the results of the tests, the graphs of dependence of UHPFRC properties on the parameter characterizing the concrete composition were plotted. A criterion that depends on the activity of the cement used as well as the effective water–cement ratio was introduced as such a parameter:

$$\varphi = \frac{R_c}{W/C_{eff}},\ [\text{Mpa}] \tag{13}$$

where

R_c is the 28 days compressive strength of Portland cement, MPa;
W/C_{eff} is the effective water–cement ratio.

The effective water–cement ratio, W/C_{eff}, is calculated as the ratio of the mass of water to the sum of the masses of cement and silica fume multiplied by the silica fume efficiency factor, K_{eff}, which indicates how many parts of cement can be replaced with silica fume to obtain the same strength. The efficiency factor of the mineral admixture is

determined experimentally. For this purpose, the compressive strength of a control mixture without additives is determined, as well as several additional ones with the replacement of a part of cement with a mineral admixture at a constant water-binder ratio $W/B = W/(C + SF)$. After determining the compressive strength of the compositions, K_{eff} is determined [69]:

$$K_{eff} = 1 + \frac{R_{rel} - 1}{p}, [-] \quad (14)$$

where

R_{rel} is the relative compressive strength of silica fume and control mixture;
p is the percentage cement replacement by silica fume in fractions of a unit.

The efficiency factor depends on the amount of cement substituted and generally decreases with increasing dosage of mineral admixture.

Table 7 presents the K_{eff} values at 28 days of age for different levels of cement replacement with silica fume in HPC and UHPC found in the literature as well as from our own preliminary tests.

Table 7. K_{eff} of silica fume for various percentage cement replacement.

№	Percentage Cement Replacement	Compressive Strength Range, MPa	K_{eff}	References
1	0.15	110–160	1.37	Author's results
2	0.25		0.94	
3	0.15		1.53	
4	0.25		1.18	
5	0.25		0.88	
6	0.30		0.80	
7	0.10	89–115	2.91	[67]
8	0.20		2.46	
9	0.25		1.99	
10	0.05	81–92	3.72	[70]
11	0.08	124–138	2.40	[71]
12	0.16	89–96	0.87	[72]
13	0.25		0.98	
14	0.16		0.99	
15	0.25		0.81	
16	0.05	96–109	2.34	[73]
17	0.10		2.31	
18	0.15		1.89	
19	0.20		1.71	
20	0.25		1.56	
21	0.05	71–72	3.35	[74]
22	0.075		2.32	
23	0.10	82–105	2.95	[75]
24	0.20		2.40	
25	0.30		1.73	
26	0.05	101–129	2.58	[76]
27	0.10		2.19	
28	0.15		2.19	
29	0.20		2.39	
30	0.25		2.03	

The graph in Figure 16 shows the relationship between the silica fume efficiency factor and the cement replacement percentage, plotted using data from Table 6.

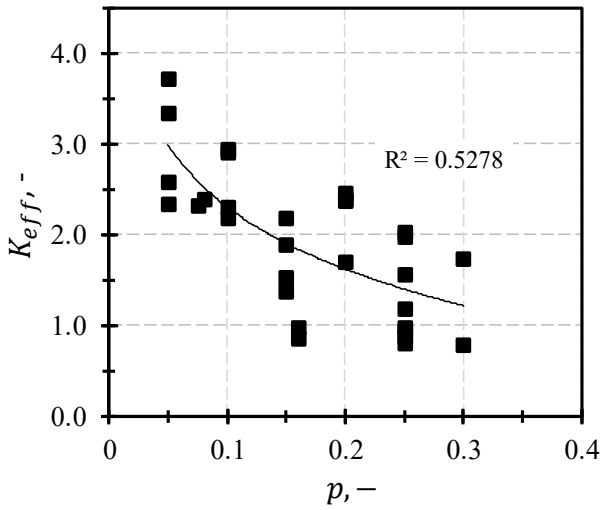


Figure 16. Efficiency factor of silica fume versus percentage cement replacement.

The experimental data were approximated by the following equation:

$$K_{eff} = -0.99 \cdot \ln(p) + 0.034\ [-] \quad (15)$$

Table 8 shows the calculated values of the coefficients φ and K_{eff} for compositions I, II and III using Equations (13) and (15).

Table 8. Calculated parameters of different UHPC mixtures.

Mix	p, -	K_{eff}.-	φ, MPa
I	0.13	2.05	266
II	0.20	1.63	309
III	0.20	1.63	401

The plots in Figure 17 show the dependence of all the properties of UHPC and UHPFRC defined in this paper on the parameter φ.

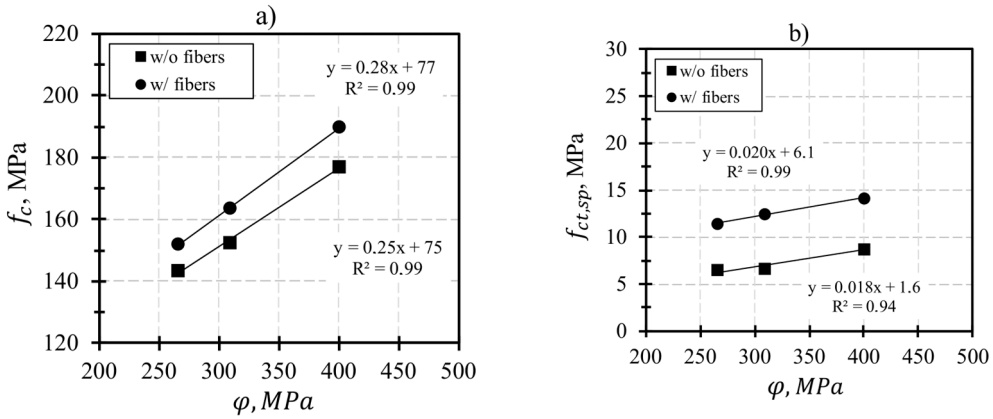


Figure 17. *Cont.*

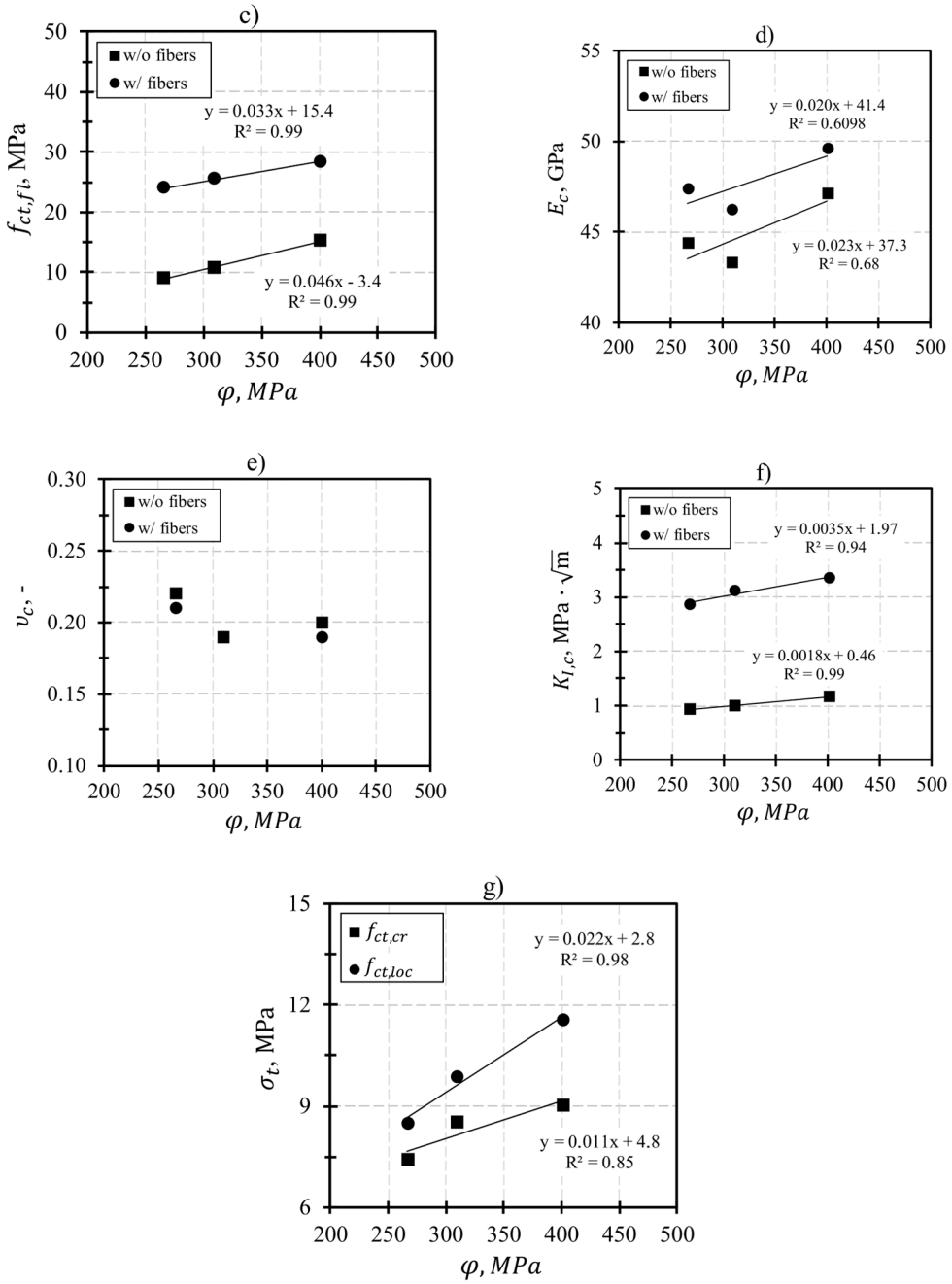


Figure 17. Properties of UHPC and UHPFRC depending on φ: (**a**) compressive strength; (**b**) splitting tensile strength; (**c**) flexural strength; (**d**) modulus of elasticity; (**e**) Poisson's coefficient; (**f**) critical stress intensity factor; (**g**) direct tensile strength.

All defined properties depend linearly on the parameter φ. The experimental data were approximated using a straight line equation ($y = a \cdot \varphi + b$). When steel fiber is introduced, the coefficient $\boldsymbol{a}$ in the equation practically does not change, resulting in a series of parallel straight lines. This fact allows us to determine the properties of UHPC/UHPFRC with any other volume content of corrugated steel fiber by the following equation:

$$Y = a \cdot \varphi + b_0 + b_1 \cdot V_f, \tag{16}$$

where

Y is the one of mechanical property of UHPC/UHPFRC from Figure 15;

b_0 is the empirical coefficient for UHPC without steel fiber;
b_1 is the increment value of coefficient b_0 per 1% of steel fiber.

The value of the coefficient a of Equation (16) was obtained as the arithmetic mean of the coefficients of equations from Figure 17 with fiber content of 0 and 2%. The value of the coefficient b_1 was determined by the following equation:

$$b_1 = \frac{b_{v_{f=2\%}} - b_{v_{f=0\%}}}{2}, \quad (17)$$

where

$b_{v_{f=2\%}}$ is the value of the coefficient b of the linear equation for the composition with 2% steel fiber;
$b_{v_{f=0\%}}$ is the value of the coefficient b of the linear equation for the composition with 0% steel fiber.

Table 9 summarizes the average values of the coefficients a, b_0 and b_1 obtained from the plots in Figure 15.

Table 9. Values of coefficients a, b_0 and b_1 from Equation (16).

Parameter	a	b_0	b_1
f_c	0.265	75	1.0
$f_{ct,sp}$	0.019	1.6	2.3
$f_{ct,fl}$	0.040	−3.4	9.4
ν_c	-	-	-
E_c	0.022	37.3	2.1
$K_{I,c}$	0.0027	0.46	0.8

The plots of Figure 18 show the comparison between experimental and calculated values of UHPC and UHPFRC properties determined from Equation (16).

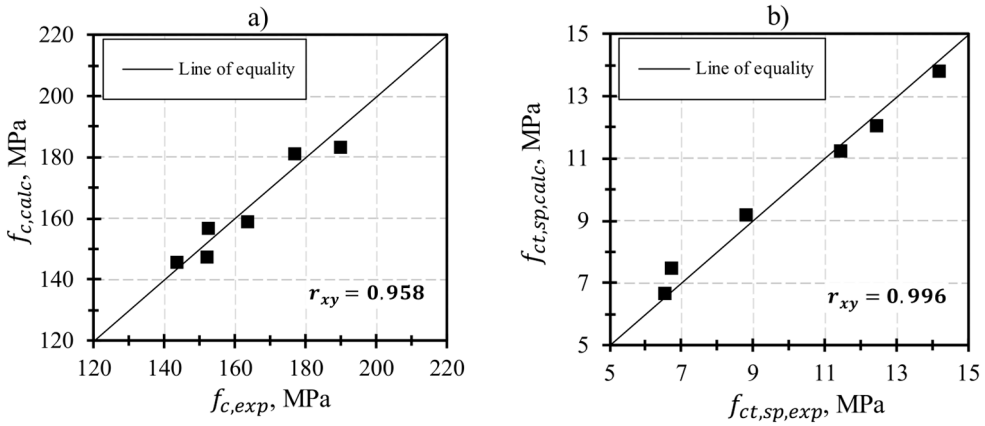


Figure 18. *Cont.*

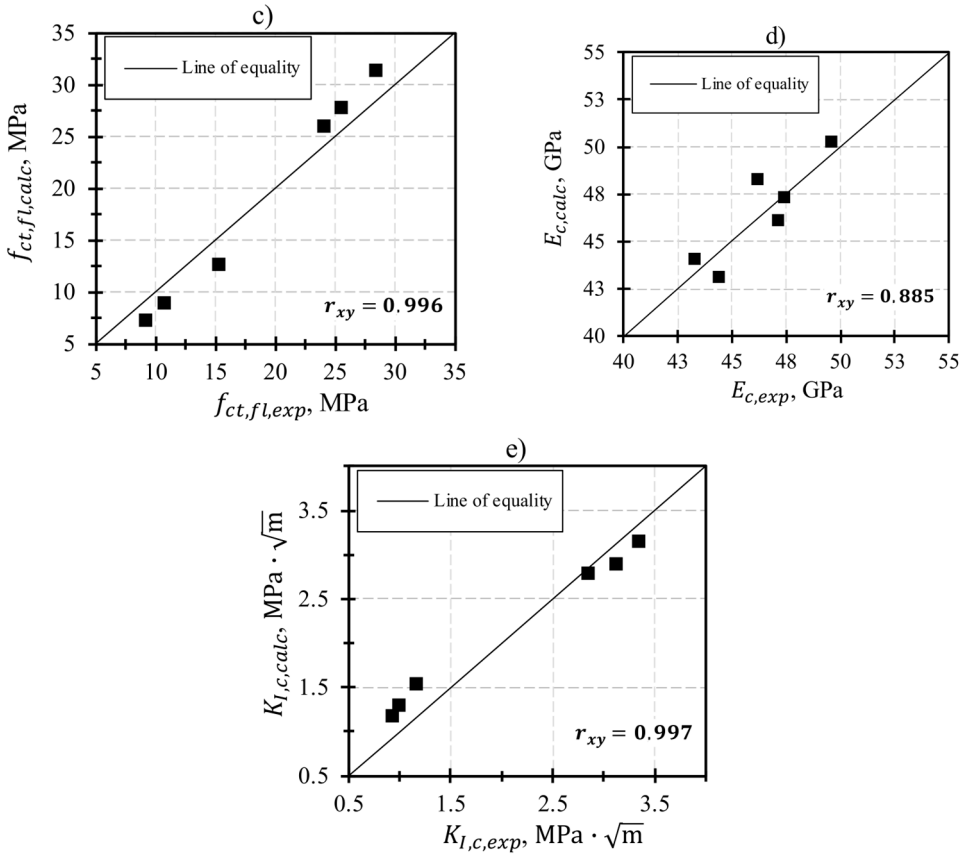


Figure 18. Comparison of experimental data with those obtained from the Equation (16): (**a**) compressive strength; (**b**) splitting tensile strength; (**c**) flexural strength; (**d**) modulus of elasticity; (**e**) critical stress intensity factor.

The correlation coefficient between experimental and calculated values is in the range of 0.885–0.997, which allows us to recommend Equation (16) for predicting the properties of UHPFRC with different volume content of corrugated steel fiber.

5. Conclusions

In this work, various mechanical characteristics of three different UHPC compositions with compressive strengths of 143, 152 and 177 MPa were determined. The influence of introducing corrugated steel fiber as the most widespread on the territory of the Russian Federation was studied. Fibers with a ratio of $l_f/d_f = 50$ and a volume content of 2% were used in this work. The conclusions from the tests performed are summarized below:

- The introduction of steel fiber slightly increases compressive strength;
- There is a sharp increase in flexural strength, splitting tensile strength and critical stress intensity factor with the introduction of steel fiber. This is due to the fact that the fiber takes up the load after the formation of a crack in the concrete matrix;
- A slight increase in elastic modulus with the introduction of steel fiber is observed, which is consistent with the well-known "rule of mixtures";
- It is found that the Poisson's ratio is independent of the strength of UHPC and the presence of steel fiber. The average value obtained in this work is 0.2;
- From the axial tensile tests carried out, it is found that an increase in UHPC compressive strength leads to a proportional increase in cracking stress and tensile strength of UHPFRC. The fracture energy during strain-hardening and during softening also increases with the increasing strength of the UHPC matrix.

Finally, simple empirical equations were derived to predict the properties of UHPC and UHPFRC as a function of water–cement ratio, silica fume content and its efficiency

factor, compressive strength of cement and volume content of corrugated steel fiber. The experimental values correlate well with the calculated ones.

In the future, a more in-depth study of the factors affecting the efficiency factor of silica fume in UHPC is needed. It is also necessary to study the properties of UHPFRC with corrugated steel fiber with other l_f/d_f ratios to obtain more general equations to predict the material properties.

Author Contributions: Conceptualization, V.S. and E.M.; methodology, V.S.; software, E.M.; validation, V.S. and E.M.; formal analysis, V.S. and E.M.; investigation, V.S. and E.M.; resources, E.M.; data curation, V.S.; writing—original draft preparation, V.S. and E.M.; writing—review and editing, V.S. and E.M.; visualization, E.M.; supervision, V.S.; project administration, V.S.; funding acquisition, V.S. All authors have read and agreed to the published version of the manuscript.

Funding: This work was financially supported by the Ministry of Science and Higher Education of Russian Federation (grant # 075-15-2021-686). Tests were carried out using research equipment of The Head Regional Shared Research Facilities of the Moscow State University of Civil Engineering.

Data Availability Statement: The data presented in this study are available upon request from the corresponding author.

Conflicts of Interest: The authors declare no conflict of interest.

References

1. Bajaber, M.A.; Hakeem, I.Y. UHPC Evolution, Development, and Utilization in Construction: A Review. *J. Mater. Res. Technol.* **2021**, *10*, 1058–1074. [CrossRef]
2. Azmee, N.M.; Shafiq, N. Ultra-High Performance Concrete: From Fundamental to Applications. *Case Stud. Constr. Mater* **2018**, *9*, e00197. [CrossRef]
3. Perry, V.; Eng, P. What Really Is Ultra-High Performance Concrete? Towards a Global Definition. In Proceedings of the 2nd International Conference on Ultra-High Performance Concrete Material & Structures, Fuzhou, China, 7–10 November 2018.
4. Perry, V.H.; Seibert, P.J. Fifteen years of UHPC construction experience in precast bridges in north America. In Proceedings of the RILEM-fib-AFGC Int. Symposium on Ultra-High Performance Fibre-Reinforced Concrete, Marseille, France, 1–3 October 2013.
5. Hajar, Z.; Resplendino, J.; Simon, A. Ultra-High-Performance Concretes: First Recommendations and Examples of Application. In Proceedings of the Concrete Structures: The Challenge of Creativity, Avignon, France, 26–28 May 2004.
6. Toutlemonde, F.; Terrade, B.; Pons, T.; Guirado, F.; Billo, J.; Renaud, J.-C.; Vidal, T.; Nicot, P.; Fourré, M.; Simon, A. 20-Years Field Durability Experience of Oldest UHPFRC Structural Elements. In Proceedings of the Hipermat, Kassel, Germany, 11–13 March 2020.
7. Zhou, J.; Li, C.; Feng, Z.; Yoo, D.Y. Experimental Investigation on Torsional Behaviors of Ul-tra-High-Performance Fiber-Reinforced Concrete Hollow Beams. *Cem. Concr. Compos.* **2022**, *129*, 104504. [CrossRef]
8. Xue, J.; Briseghella, B.; Huang, F.; Nuti, C.; Tabatabai, H.; Chen, B. Review of Ultra-High Performance Concrete and Its Application in Bridge Engineering. *Constr. Build Mater.* **2020**, *260*, 119844. [CrossRef]
9. Mash, J.A.; Harries, K.A.; Rogers, C. Repair of corroded steel bridge girder end regions using steel, concrete, UHPC and GFRP repair systems. *J. Constr. Steel Res.* **2023**, *207*, 107975. [CrossRef]
10. Hung, C.-C.; El-Tawil, S.; Chao, S.-H. A Review of Developments and Challenges for UHPC in Structural Engineering: Behavior, Analysis, and Design. *J. Struct. Eng.* **2021**, *147*, 03121001. [CrossRef]
11. Sharma, R.; Jang, J.G.; Bansal, P.P. A Comprehensive Review on Effects of Mineral Admixtures and Fibers on Engineering Properties of Ultra-High-Performance Concrete. *J. Build. Eng.* **2022**, *45*, 103314. [CrossRef]
12. Parant, E.; Rossi, P.; Boulay, C. Fatigue Behavior of a Multi-Scale Cement Composite. *Cem. Concr. Res.* **2007**, *37*, 264–269. [CrossRef]
13. Rossi, P.; Arca, A.; Parant, E.; Fakhri, P. Bending and Compressive Behaviours of a New Cement Composite. *Cem. Concr. Res.* **2005**, *35*, 27–33. [CrossRef]
14. Benson, S.D.P.; Karihaloo, B.L. CARDIFRC®—Development and Mechanical Properties. Part I: Development and Workability. *Mag. Concr. Res.* **2005**, *57*, 347–352. [CrossRef]
15. Nicolaides, D.; Benson, S.D.P.; Nicolaides, D.; Karihaloo, B.L. CARDIFRC-Development and Mechanical Properties. Part II: Fibre Distribution. *Mag. Concr. Res.* **2015**, *57*, 421–432.
16. Benson, S.D.P.; Karihaloo, B.L. CARDIFRC®—Development and Mechanical Properties. Part III: Uniaxial Tensile Response and Other Mechanical Properties. *Mag. Concr. Res.* **2005**, *57*, 433–443. [CrossRef]
17. Farhat, F.A.; Nicolaides, D.; Kanellopoulos, A.; Karihaloo, B.L. High Performance Fibre-Reinforced Cementitious Composite (CARDIFRC)—Performance and Application to Retrofitting. *Eng. Fract. Mech.* **2007**, *74*, 151–167. [CrossRef]
18. Yu, R.; Spiesz, P.; Brouwers, H.J.H. Mix Design and Properties Assessment of Ultra-High Performance Fibre Reinforced Concrete (UHPFRC). *Cem. Concr. Res.* **2014**, *56*, 29–39. [CrossRef]

19. Yang, J.; Chen, B.; Nuti, C. Influence of Steel Fiber on Compressive Properties of Ultra-High Performance Fiber-Reinforced Concrete. *Constr. Build. Mater.* **2021**, *302*, 124104. [CrossRef]
20. Zhu, H.; Li, C.; Gao, D.; Yang, L.; Cheng, S. Study on Mechanical Properties and Strength Relation between Cube and Cylinder Specimens of Steel Fiber Reinforced Concrete. *Adv. Mech. Eng.* **2019**, *11*, 1–12. [CrossRef]
21. Prabha, L.S.; Dattatreya, J.K.; Neelamegan, M.; Shehagiri Rao, M.V. study on stress-strain properties of reactive powder concrete under uniaxial compression. *Int. J. Eng. Res. Technol.* **2010**, *2*, 6408–6416.
22. Pourbaba, M.; Asefi, E.; Sadaghian, H.; Mirmiran, A. Effect of Age on the Compressive Strength of Ultra-High-Performance Fiber-Reinforced Concrete. *Constr. Build. Mater.* **2018**, *175*, 402–410. [CrossRef]
23. Savino, V.; Lanzoni, L.; Tarantino, A.M.; Viviani, M. Simple and Effective Models to Predict the Compressive and Tensile Strength of HPFRC as the Steel Fiber Content and Type Changes. *Compos. B Eng.* **2018**, *137*, 153–162. [CrossRef]
24. Kazemi, S.; Lubell, A.S. Influence of Specimen Size and Fiber Content on Mechanical Properties of Ultra-High-Performance Fiber-Reinforced Concrete. *ACI Mater. J.* **2012**, *109*, 675–684.
25. Oh, B.H.; Choi, O.C.; Chung, L. Phusical and mechanical properties of ultra high strength fiber reinforced cementitious composites. In Proceedings of the 7th International Conference on Fracture Mechanics of Concrete and Concrete Structures, Jeju, Republic of Korea, 23–28 May 2010.
26. Zhang, S.S.; Wang, J.J.; Lin, G.; Yu, T.; Fernando, D. Stress-Strain Models for Ultra-High Performance Concrete (UHPC) and Ultra-High Performance Fiber-Reinforced Concrete (UHPFRC) under Triaxial Compression. *Constr. Build. Mater.* **2023**, *370*, 130658. [CrossRef]
27. Yang, J.; Chen, B.; Wu, X.; Xu, G. Quantitative Analysis of Steel Fibers on UHPFRC Uniaxial Tensile Behavior Using X-CT and UTT. *Constr. Build. Mater.* **2023**, *368*, 130349. [CrossRef]
28. Paschalis, S.; Lampropoulos, A. Fiber Content and Curing Time Effect on the Tensile Characteristics of Ultra High Performance Fiber Reinforced Concrete. *Struct. Concr.* **2017**, *18*, 577–588. [CrossRef]
29. Wille, K.; El-Tawil, S.; Naaman, A.E. Properties of Strain Hardening Ultra High Performance Fiber Reinforced Concrete (UHP-FRC) under Direct Tensile Loading. *Cem. Concr. Compos.* **2014**, *48*, 53–66. [CrossRef]
30. Pyo, S.; Wille, K.; El-Tawil, S.; Naaman, A.E. Strain Rate Dependent Properties of Ultra High Performance Fiber Reinforced Concrete (UHP-FRC) under Tension. *Cem. Concr. Compos.* **2015**, *56*, 15–24. [CrossRef]
31. Wille, K.; Naaman, A.E.; El-Tawil, S. Optimizing Ultra-High-Performance Fiber-Reinforced Concrete Mixtures with Twisted Fibers Exhibit Record Performance under Tensile Loading. *ACI Concr. Int.* **2011**, *33*, 35–41.
32. Abellán-García, J. Tensile Behavior of Recycled-Glass-UHPC under Direct Tensile Loading. *Case Stud. Constr. Mater.* **2022**, *17*, e01308. [CrossRef]
33. Abrishambaf, A.; Pimentel, M.; Nunes, S. Influence of Fibre Orientation on the Tensile Behaviour of Ultra-High Performance Fibre Reinforced Cementitious Composites. *Cem. Concr. Res.* **2017**, *97*, 28–40. [CrossRef]
34. Xu, M.; Wille, K. Fracture Energy of UHP-FRC under Direct Tensile Loading Applied at Low Strain Rates. *Compos. B Eng.* **2015**, *80*, 116–125. [CrossRef]
35. Wille, K.; Kim, D.J.; Naaman, A.E. Strain-Hardening UHP-FRC with Low Fiber Contents. *Mater. Struct.* **2011**, *44*, 583–598. [CrossRef]
36. Huang, H.; Gao, X.; Khayat, K.H. Contribution of Fiber Alignment on Flexural Properties of UHPC and Prediction Using the Composite Theory. *Cem. Concr. Compos.* **2021**, *118*, 103971. [CrossRef]
37. Yoo, D.Y.; Kim, S.; Park, G.J.; Park, J.J.; Kim, S.W. Effects of Fiber Shape, Aspect Ratio, and Volume Fraction on Flexural Behavior of Ultra-High-Performance Fiber-Reinforced Cement Composites. *Compos. Struct.* **2017**, *174*, 375–388. [CrossRef]
38. Yoo, D.Y.; Kim, M.J.; Kim, S.W.; Park, J.J. Development of Cost Effective Ultra-High-Performance Fiber-Reinforced Concrete Using Single and Hybrid Steel Fibers. *Constr. Build. Mater.* **2017**, *150*, 383–394. [CrossRef]
39. Alsalman, A.; Dang, C.N.; Prinz, G.S.; Hale, W.M. Evaluation of Modulus of Elasticity of Ultra-High Performance Concrete. *Constr. Build. Mater.* **2017**, *153*, 918–928. [CrossRef]
40. Xu, Y.; Liu, J.; Liu, J.; Zhang, P.; Zhang, Q.; Jiang, L. Experimental Studies and Modeling of Creep of UHPC. *Constr. Build. Mater.* **2018**, *175*, 643–652. [CrossRef]
41. Shehab El-Din, H.K.; Mohamed, H.A.; Abd El-HakKhater, M.; Ahmed, S.; Abd El-Hak Khater, M. Effect of Steel Fibers on Behavior of Ultra High Performance Concrete. In Proceedings of the First International Interactive Symposium on UHPC, Des Moines, IA, USA, 18–20 July 2016.
42. Yoo, D.Y.; Park, J.J.; Kim, S.W. Fiber Pullout Behavior of HPFRCC: Effects of Matrix Strength and Fiber Type. *Compos. Struct.* **2017**, *174*, 263–276. [CrossRef]
43. Kang, S.H.; Ahn, T.H.; Kim, D.J. Effect of Grain Size on the Mechanical Properties and Crack Formation of HPFRCC Containing Deformed Steel Fibers. *Cem. Concr. Res.* **2012**, *42*, 710–720. [CrossRef]
44. Kim, J.J.; Yoo, D.Y. Effects of Fiber Shape and Distance on the Pullout Behavior of Steel Fibers Embedded in Ultra-High-Performance Concrete. *Cem. Concr. Compos.* **2019**, *103*, 213–223. [CrossRef]
45. Wille, K.; Naaman, A.E. Effect of Ultra-High-Performance Concrete on Pullout Behavior of High-Strength Brass-Coated Straight Steel Fibers. *ACI Mater. J.* **2013**, *110*, 451–462.
46. Lowke, D.; Stengel, T.; Gehlen, C. Control of Rheology, Strength and Fibre Bond of UHPC with Additions-Effect of Packing Density and Addition Type. In Proceedings of the Ultra-High Performance Concrete and Nanotechnology in Construction, Kassel, Germany, 7–9 March 2012.

47. Qi, J.; Wu, Z.; Ma, Z.J.; Wang, J. Pullout Behavior of Straight and Hooked-End Steel Fibers in UHPC Matrix with Various Embedded Angles. *Constr. Build. Mater.* **2018**, *191*, 764–774. [CrossRef]
48. Zhang, H.; Ji, T.; Lin, X. Pullout Behavior of Steel Fibers with Different Shapes from Ultra-High Performance Concrete (UHPC) Prepared with Granite Powder under Different Curing Conditions. *Constr. Build. Mater.* **2019**, *211*, 688–702. [CrossRef]
49. de Larrard, F. *Concrete Mixture Proportioning: A Scientific Approach*; E. & F.N. Spon: London, UK, 1999; pp. 1–76.
50. Moutassem, F. Assessment of Packing Density Models and Optimizing Concrete Mixtures. *IJCMES* **2016**, *2*, 29–36.
51. Gong, C.; Kang, L.; Liu, L.; Lei, M.; Ding, W.; Yang, Z. A Novel Prediction Model of Packing Density for Single and Hybrid Steel Fiber-Aggregate Mixtures. *Powder Technol.* **2023**, *418*, 118295. [CrossRef]
52. *GOST 10180–2012*; Concretes: Methods for Strength Determination Using Reference Specimens. Russian Standardization Institute: Moscow, Russia, 2018.
53. *GOST 24452-80*; Concretes: Methods of Prismatic, Compressive Strength, Modulus of Elasticity and Poisson's Ratio Determination. Russian Standardization Institute: Moscow, Russia, 2005.
54. *GOST 29167-2021*; Concretes: Methods for Determining Crack Resistance (Fracture Toughness) Characteristics under Static Loading. Russian Standardization Institute: Moscow, Russia, 2022.
55. Abrishambaf, A.; Pimentel, M.; Nunes, S. A Meso-Mechanical Model to Simulate the Tensile Behaviour of Ultra-High Performance Fibre-Reinforced Cementitious Composites. *Compos. Struct.* **2019**, *222*, 110911. [CrossRef]
56. Nežerka, V.; Bílý, P.; Hrbek, V.; Fládr, J. Impact of Silica Fume, Fly Ash, and Metakaolin on the Thickness and Strength of the ITZ in Concrete. *Cem. Concr. Compos.* **2019**, *103*, 252–262. [CrossRef]
57. Jiao, C.; Ta, J.; Niu, Y.; Mengg, S.; Chen, X.F.; He, S.; Ma, R. Analysis of the Flexural Properties of Ultra-High-Performance Concrete Consisting of Hybrid Straight Steel Fibers. *Case Stud. Constr. Mater.* **2022**, *17*, e01153. [CrossRef]
58. Mostofinejad, D.; Mostofinejad, D.; Nozhati, M. Prediction of the Modulus of Elasticity of High Strength Concrete. *Iran. J. Sci. Technol. B* **2005**, *29*, 311–321.
59. Alsalman, A.; Kareem, R.; Dang, C.N.; Martí-Vargas, J.R.; Micah Hale, W. Prediction of Modulus of Elasticity of UHPC Using Maximum Likelihood Estimation Method. *Structures* **2022**, *35*, 1308–1320. [CrossRef]
60. Kim, J.C.; Lim, W.Y. Prediction of Compressive Strength and Elastic Modulus for Ultra-High-Performance Concrete. *Constr. Build. Mater.* **2023**, *363*, 129883. [CrossRef]
61. El-Helou, R.G.; Haber, Z.B.; Graybeal, B.A. Mechanical Behavior and Design Properties of Ultra-High-Performance Concrete. *ACI Mater. J.* **2022**, *119*, 181–194. [CrossRef]
62. Kan, Y.C.; Pei, K.C.; Chang, C.L. Strength and Fracture Toughness of Heavy Concrete with Various Iron Aggregate Inclusions. *Nucl. Eng. Des.* **2004**, *228*, 119–127. [CrossRef]
63. Wu, C.H.; Huang, C.H.; Kan, Y.C.; Yen, T. Effects of Fineness and Dosage of Fly Ash on the Fracture Properties and Strength of Concrete. *Appl. Sci.* **2019**, *9*, 2266. [CrossRef]
64. Lange-Kornbak, D.; Karihaloo, B.L. Design of Fiber-Reinforced DSP Mixes for Minimum Brittleness. *Adv. Cem. Bas. Mat.* **1998**, *7*, 89–101. [CrossRef]
65. Hoseini, S.O.; Sohrabi, M.R.; Mousavi, S.R.; Ghasemi, M. Effects of Coarse Aggregate and Wavy Steel Fiber Volumes on the Critical Stress Intensity Factors of Modes I and III Cracks in Self-Compacting Concrete Using ENDB Specimens. *Theor. Appl. Fract. Mech.* **2022**, *121*, 103421. [CrossRef]
66. Jungwirth, J. On the Tensile Load-Bearing Behavior of Ultra-High-Performance Fiber-Reinforced Concrete Structural Members. Ph.D. Thesis, Ecole Polytechnique Fédérale de Lausanne, Lausanne, Switzerland, 2006.
67. Wu, Z.; Shi, C.; Khayat, K.H. Influence of Silica Fume Content on Microstructure Development and Bond to Steel Fiber in Ultra-High Strength Cement-Based Materials (UHSC). *Cem. Concr. Compos.* **2016**, *71*, 97–109. [CrossRef]
68. Pi, Z.; Xiao, H.; Liu, R.; Li, H. Combination Usage of Nano-SiO_2-Coated Steel Fiber and Silica Fume and Its Improvement Effect on SFRCC. *Compos. B Eng.* **2021**, *221*, 109022. [CrossRef]
69. Le, H.T.; Müller, M.; Siewert, K.; Ludwig, H.M. The Mix Design for Self-Compacting High Performance Concrete Containing Various Mineral Admixtures. *Mater. Des.* **2015**, *72*, 51–62. [CrossRef]
70. Shihada, M.; Arafa, M. Effects of Silica Fume, Ultrafine and Mixing Sequences on Properties of Ultra High Performance Concrete. *Asian J. Mater. Sci.* **2010**, *2*, 137–146. [CrossRef]
71. Paredes, J.A.; Gálvez, J.C.; Enfedaque, A.; Alberti, M.G. Matrix Optimization of Ultra High Performance Concrete for Improving Strength and Durability. *Materials* **2021**, *14*, 6944. [CrossRef]
72. Toutanji, H.A.; El-Korchi, T. The influence of silica fume on the compressive strength of cement paste and mortar. *Cem. Concr. Res.* **1995**, *25*, 1591–1602. [CrossRef]
73. Smarzewski, P. Influence of Silica Fume on Mechanical and Fracture Properties of High Performance Concrete. *Procedia Struct. Integr.* **2019**, *17*, 5–12. [CrossRef]
74. Nili, M.; Ehsani, A. Investigating the Effect of the Cement Paste and Transition Zone on Strength Development of Concrete Containing Nanosilica and Silica Fume. *Mater. Des.* **2015**, *75*, 174–183. [CrossRef]

75. Zhang, Y.; Chang, J.; Zhao, Q.; Lam, W.L.; Shen, P.; Sun, Y.; Zhao, D.; Poon, C.S. Effect of Dosage of Silica Fume on the Macro-Performance and Micro/Nanostructure of Seawater Portland Cement Pastes Prepared with an Ultra-Low Water-to-Binder Ratio. *Cem. Concr. Compos.* **2022**, *133*, 104700. [CrossRef]
76. Xu, D.; Tang, J.; Hu, X.; Zhou, Y.; Yu, C.; Han, F.; Liu, J. Influence of Silica Fume and Thermal Curing on Long-Term Hydration, Microstructure and Compressive Strength of Ultra-High Performance Concrete (UHPC). *Constr. Build. Mater.* **2023**, *395*, 132370. [CrossRef]

Disclaimer/Publisher's Note: The statements, opinions and data contained in all publications are solely those of the individual author(s) and contributor(s) and not of MDPI and/or the editor(s). MDPI and/or the editor(s) disclaim responsibility for any injury to people or property resulting from any ideas, methods, instructions or products referred to in the content.